A Model Predictive Direct Current Control Strategy with Predictive References for MV Grid-Connected Converters with LCL-Filters

James Scoltock, *Student Member, IEEE,* Tobias Geyer, *Senior Member, IEEE,* and Udaya K. Madawala, *Senior Member, IEEE*

***Abstract*—In this paper, a new model predictive direct current control (MPDCC) strategy is proposed for a medium-voltage (MV) neutral-point-clamped converter with an LCL-filter-based connection to the grid. The proposed strategy addresses the issues of resonance damping and harmonic attenuation through the virtual resistor (VR) concept, and is thus termed MPDCC-VR. Because MPDCC is capable of achieving very long prediction horizons, the VR-based reference terms are predicted in conjunction with the state trajectories at each time-step, thus enabling more accurate decisions to be made by the controller. Simulation results verify the applicability of MPDCC-VR to a MV case study. It is shown that the proposed approach exhibits a very good level of steady-state performance in the presence of grid voltage distortion, and at the chosen operating point is capable of substantially outperforming multi-loop control with space vector modulation. Experimental results, which are provided for a down-scaled prototype, show excellent agreement with those obtained in simulation, further validating the proposed MPDCC-VR strategy.**

***Index Terms*—Current control, grid-connected converter, LCL-filter, model predictive control, neutral-point-clamped converter**

NOMENCLATURE

u_{abc}	Converter switching state vector.
v	Converter output voltage vector.
i	Converter current vector.
i_g	Grid current vector.
v_c	Capacitor voltage vector.
v_g	Grid voltage vector.
v_n	Neutral-point potential.
δ_i	Converter current bound width.
i_f^*	Fundamental converter current reference.
i_{vr}^*	Resonance damping converter current reference.
i_{vh}^*	Harmonic attenuation converter current reference.
R_{vr}	Virtual resonance damping resistor.
R_{vh}	Virtual harmonic attenuation resistor.

This work was supported in part by The University of Auckland Doctoral Scholarship.

J. Scoltock and U.K. Madawala are with the Department of Electrical and Computer Engineering, The University of Auckland, 1010 Auckland, New Zealand (email: jsco075@aucklanduni.ac.nz, u.madawala@auckland.ac.nz).

T. Geyer is with ABB Corporate Research, 5405 Baden-Dättwil, Switzerland (email: t.geyer@ieee.org).

I. INTRODUCTION

In recent years, Model Predictive Control (MPC) has gained substantial attention within the power electronics community [1], [2]. Among the main advantages of MPC are the ability to handle input, state and output constraints, multiple inputs and outputs, and non-linear dynamics in a straightforward manner [2]. Among the most commonly reported applications of MPC in power electronics are machine drives [3]–[5], standalone inverters [6], and converters which are connected to the grid through a series inductor (sometimes referred to as an 'L-filter') [7], [8]. Although several variants of MPC have been developed within power electronics, the Finite Control Set-MPC (FCS-MPC) approach has become the best-known [1], [2]. FCS-MPC is formulated without a PWM stage, instead approaching the control task as an on-line optimisation problem, with the switching state that is predicted to minimise a given cost function applied to the converter at each time-step [9]. Although typically formulated with a prediction horizon of one time-step [1], it has recently been shown that by adopting the appropriate mathematical programming techniques, the prediction horizon can be extended over multiple time-steps without the computational burden becoming excessive [10], [11].

An alternative MPC-based approach has also emerged in parallel with FCS-MPC. Model Predictive Direct Torque Control (MPDTC), presented in [3], [12]–[14], was developed specifically for the control of Medium-Voltage (MV) Induction Machine (IM) drives. Like FCS-MPC, MPDTC directly controls the switching state of the converter. However, by regulating the output variables within a given set of bounds, and by utilising the concept of trajectory extension, MPDTC is able to achieve long prediction horizons. Consequently, very low device switching frequencies can be achieved, making MPDTC very well-suited to MV applications [3], [12]–[17]. A natural extension of MPDTC is Model Predictive Direct Current Control (MPDCC), which in the context of an IM directly regulates the stator currents [16]–[18].

In grid-connected applications, LCL-filters are of significant interest due to the high level of harmonic attenuation that is offered relative to series inductors. In MV applications, such filters are of particular importance, as the higher level of harmonic attenuation that is offered may enable the converter

to operate at a lower switching frequency than is possible with a series inductor, whilst operating within acceptable harmonic limits. The main challenge in the development of suitable control strategies for LCL-filter-based setups include the damping of the resonant frequency(ies) of the filter. To date, the issue of resonance damping has mainly been addressed through Multi-Loop Control (MLC) [19], [20], Virtual Resistance (VR) [21], [22], and filter-based [23], [24] Active Damping (AD) concepts. Although passive (resistor-based) damping is also possible, the reduced efficiency make AD solutions preferable. An additional challenge is the mitigation of grid voltage harmonics, which can degrade the performance of the system if not adequately compensated for [19], [25].

Although a number of papers have proposed MPC strategies for Low-Voltage (LV) grid-connected converters with LCL-filters, see e.g. [26], [27], very few works to date have addressed the problem of developing such strategies for MV converters. In [28], a FCS-MPC-based current control strategy is developed for a Neutral-Point-Clamped (NPC) converter with an LCL-filter. The proposed strategy incorporates tuned digital filters to address the issue of resonance damping, and for the chosen case-study the switching frequency of the converter was approximately 1 kHz. In [29], a predictive current controller was proposed for a similarly-rated NPC converter-based system, with the main advantage of the proposed strategy being improved performance in the presence of grid faults. Both [28] and [29] feature a short prediction horizon of one time-step. In [30], a similar problem, namely the development of an MPC strategy for a MV IM drive with an LC-filter, was addressed. The proposed strategy was based on an early iteration of the MPDTC algorithm, and incorporated the VR concept in order to damp the resonance of the filter. The proposed strategy was shown to achieve lower switching losses than conventional DTC.

In this paper, we present a new MPDCC strategy for the control of MV grid-connected NPC converters with LCL-filters. The proposed strategy addresses the issues of resonance damping and harmonic attenuation through the VR concept, and is thus termed MPDCC-VR. Unlike the strategies proposed in [28], [29], MPDCC is capable of achieving very long prediction horizons. As such, the VR-based reference terms are predicted in conjunction with the predicted state trajectories at each time-step, enabling more accurate decisions to be made by the controller. The key benefit of the proposed strategy is the fact that very low switching frequencies can be achieved in conjunction with high levels of resonance damping and harmonic attenuation, allowing the converter to operate within acceptable harmonic limits, i.e. those specified by IEEE Std. 519 [31], even in the presence of grid voltage distortion.

Simulation results verify the applicability of MPDCC-VR to a MV case study, and it is shown that MPDCC-VR achieves switching frequencies as low as 300 Hz whilst operating within the limits specified by IEEE Std. 519. The steady-state performance of MPDCC-VR is also compared against that of MLC with Space Vector Modulation (SVM), and at the chosen operating point, it is shown that MPDCC-VR offers a switching frequency which improves upon MLC with SVM by between 23.6% and 34.9%. Experimental results are presented in order to verify the practical viability of MPDCC-VR. The performance of the down-scaled prototype shows excellent agreement with the results obtained in simulation, further validating the MPDCC-VR strategy.

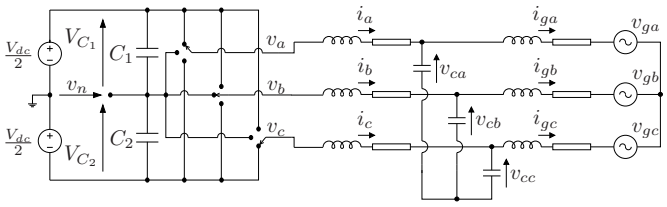

Fig. 1: Representation of a three-phase neutral-point-clamped converter connected to the grid via an LCL-filter.

II. Setup and Control Problem

A. Setup

A representation of the system under consideration, which consists of a three-phase NPC converter connected to the grid via an LCL-filter, is shown in Fig. 1. The converter switching state is denoted

$$u_{abc} = [u_a \ u_b \ u_c]^T \in \{-1, \ 0, \ 1\}^3. \tag{1}$$

The sum of the voltages across the upper and lower capacitors is equal to the total DC-link voltage, i.e. $V_{dc} = V_{C_1} + V_{C_2}$. The neutral-point potential, which is defined relative to the mid-point of the DC-link, is given by $v_n = (V_{C_2} - V_{C_1})/2$, which under balanced conditions, when $V_{C_1} = V_{C_2}$, is zero.

The three-phase converter current, grid current, capacitor voltage and grid voltage vectors are defined as $i_{abc} = [i_a \ i_b \ i_c]^T$, $i_{g,abc} = [i_{ga} \ i_{gb} \ i_{gc}]^T$, $v_{c,abc} = [v_{ca} \ v_{cb} \ v_{cc}]^T$ and $v_{g,abc} = [v_{ga} \ v_{gb} \ v_{gc}]^T$, respectively. Variables $\xi_{abc} = [\xi_a \ \xi_b \ \xi_c]^T$ in the three-phase abc reference frame are transformed to $\xi = [\xi_\alpha \ \xi_\beta]^T$ in the orthogonal $\alpha\beta$ reference frame through

$$\xi = \frac{2}{3} P \xi_{abc} \tag{2}$$

where P is the transformation matrix

$$P = \begin{bmatrix} 1 & -\frac{1}{2} & -\frac{1}{2} \\ 0 & \frac{\sqrt{3}}{2} & -\frac{\sqrt{3}}{2} \end{bmatrix}. \tag{3}$$

Conversely, ξ can be transformed to ξ_{abc} via

$$\xi_{abc} = P^T \xi. \tag{4}$$

The $\alpha\beta$-frame converter current, grid current, capacitor voltage and grid voltage vectors are denoted $i = [i_\alpha \ i_\beta]^T$, $i_g = [i_{g\alpha} \ i_{g\beta}]^T$, $v_c = [v_{c\alpha} \ v_{c\beta}]^T$ and $v_g = [v_{g\alpha} \ v_{g\beta}]^T$, respectively.

B. Control Problem

The aim of the controller is to control the grid currents such that the real and reactive power delivered to and/or drawn from the grid are regulated to their desired values. For the LCL-filter-based setup under consideration, the proposed MPDCC-VR strategy achieves this implicitly, by directly controlling the converter currents.

Within the MPDCC framework, each output current is regulated within a symmetrical set of bounds defined about its respective reference [18]. This results in the output currents having a relatively flat harmonic spectrum, with the width of the current bound, denoted δ_i, being approximately proportional to the harmonic distortion of the output currents. However, inspection of the s-domain transfer function relating the grid current $i_g(s)$ to the converter current $i(s)$, given by

$$\frac{i_g(s)}{i(s)} = \frac{1}{s^2 L_g C + s R_g C + 1} \tag{5}$$

where C is the filter capacitance, L_g is the grid-side inductance and R_g is the grid-side resistance, reveals that a resonant frequency between the converter- and grid-side currents emerges at

$$f_1 = \frac{1}{2\pi}\sqrt{\frac{1}{L_g C}} \text{ Hz}. \tag{6}$$

At f_1, the gain between the converter- and grid-side currents is very high, being limited only by the series resistance of the filter inductors. Consequently, if the conventional MPDCC algorithm was directly applied to the control of the converter currents, the resonant frequency f_1 would be excited, with significant harmonic distortion being present in the currents delivered to the grid as a result. Consequently, the MPDCC-VR strategy is developed such that harmonic content in the vicinity of f_1 is eliminated from the converter currents.

Because the neutral-point potential of the converter varies with the switching state and converter currents, it also needs to be regulated within a set of bounds, the width of which is denoted δ_{v_n}. Directly regulating the neutral-point potential is standard for MPC-based strategies for NPC/diode-clamped converters, see e.g. [3]. Consequently, an overall output vector y, containing the variables to be directly controlled, can be defined as [1]

$$y = [i_{abc}^T \; v_n]^T = [i_a \; i_b \; i_c \; v_n]^T. \tag{7}$$

MPDCC-VR also aims to minimise the average device switching frequency of the converter. In MV NPC converter applications, where MV-Insulated Gate Bipolar Transistors (IGBT) and Integrated Gate-Commutated Thyristors (IGCT) are the main devices, the switching frequency is usually limited to no more than 500 Hz.

III. Model Predictive Direct Current Control Strategy

A. Internal Control Model

In order for the controller to be able to predict the trajectories of the output variables in response to input sequences, a discrete-time internal control model is required. As a first step, the converter needs to be modelled. The continuous-time dynamics of the neutral-point potential, v_n, depend on the switching state, u_{abc}, and the converter currents, i_{abc}, and can be described according to

$$\frac{dv_n}{dt} = \frac{1}{2C_{dc}} |u_{abc}|^T i_{abc} \tag{8}$$

where $C_1, C_2 = C_{dc}$ and $|u_{abc}| = [|u_a| \; |u_b| \; |u_c|]^T$. For a three-wire system, such that $i_a + i_b + i_c \triangleq 0$, v_n is only affected when one or two of the switching states are equal to zero.

The converter switching-state, u_{abc}, can be related to the output voltage at the terminals of the converter, $v_{abc} = [v_a \; v_b \; v_c]^T$, via

$$v_m = \begin{cases} \frac{u_m V_{dc}}{2} & \text{if} \quad u_m \in \{-1, 1\} \\ v_n & \text{if} \quad u_m = 0 \end{cases}, \quad m \in \{a, b, c\} \tag{9}$$

where v_a, v_b and v_c are defined relative to the mid-point of the DC-link. Subsequently, v_{abc} can be converted to the $\alpha\beta$-frame, yielding $v = [v_\alpha \; v_\beta]^T$, through

$$v = \frac{2}{3} P v_{abc}. \tag{10}$$

For the sake of brevity, a function mapping u_{abc} to v will be denoted $v = f_v(u_{abc}, V_{dc}, v_n)$.

Next, the continuous-time dynamics of the currents and voltages within the filter can be modelled. By defining the state vector x as being composed of the $\alpha\beta$-frame converter current, grid current, capacitor voltage and grid voltage vectors, respectively, such that

$$x = [i^T \; i_g^T \; v_c^T \; v_g^T]^T = [i_\alpha \; i_\beta \; i_{g\alpha} \; i_{g\beta} \; v_{c\alpha} \; v_{c\beta} \; v_{g\alpha} \; v_{g\beta}]^T \tag{11}$$

the state-equation can be written as

$$\frac{dx}{dt} = Ax + Bv = Ax + B f_v(u_{abc}, V_{dc}, v_n) \tag{12}$$

where the matrices A and B are given by

$$A = \begin{bmatrix} \frac{-R}{L} & 0 & 0 & 0 & \frac{-1}{L} & 0 & 0 & 0 \\ 0 & \frac{-R}{L} & 0 & 0 & 0 & \frac{-1}{L} & 0 & 0 \\ 0 & 0 & \frac{-R_g}{L_g} & 0 & \frac{1}{L_g} & 0 & \frac{-1}{L_g} & 0 \\ 0 & 0 & 0 & \frac{-R_g}{L_g} & 0 & \frac{1}{L_g} & 0 & \frac{-1}{L_g} \\ \frac{1}{C} & 0 & \frac{-1}{C} & 0 & 0 & 0 & 0 & 0 \\ 0 & \frac{1}{C} & 0 & \frac{-1}{C} & 0 & 0 & 0 & 0 \\ 0 & 0 & 0 & 0 & 0 & 0 & 0 & -\omega \\ 0 & 0 & 0 & 0 & 0 & 0 & \omega & 0 \end{bmatrix} \tag{13}$$

$$B = \begin{bmatrix} \frac{1}{L} & 0 & 0 & 0 & 0 & 0 & 0 & 0 \\ 0 & \frac{1}{L} & 0 & 0 & 0 & 0 & 0 & 0 \end{bmatrix}^T \tag{14}$$

where L and R are the converter-side inductance and resistance, respectively, C, L_g and R_g are as defined in the previous section, and $\omega = 2\pi f$, where f is the frequency of the grid.

In order to serve as a useful prediction model for the controller, the continuous-time model needs to be converted to discrete-time, within which $k \in \mathbb{N}_0$ denotes the current time-step and T_s denotes the sampling interval. Due to the

[1] Alternatively, the output vector can be defined in terms of the $\alpha\beta$-frame currents, although with symmetrical bounds this approach has been stated to offer a slightly lower performance than the abc-frame definition [18].

differing nature of the dynamics of the neutral-point potential and the filter states (see (8) and (12)), we utilise two coupled discrete-time models. The first describes the non-linear discrete-time dynamics of the neutral-point potential and is based on forward-Euler discretisation. By recalling (4), (8) and (11) and noting that

$$\frac{dv_n}{dt} \approx \frac{1}{T_s}(v_n(k+1) - v_n(k)) \tag{15}$$

it is possible to state that

$$v_n(k+1) = \frac{T_s}{2C_{dc}}|u_{abc}(k)|^T[P^T \ 0_{3\times 6}]x(k) + v_n(k) \tag{16}$$

with $u_{abc}(k)$ and $x(k)$ defined in the same manner as (1) and (11) and where $0_{3\times 6}$ denotes the 3 x 6 zero matrix. The linear dynamics described by (12) can be discretised according to

$$x(k+1) = Fx(k) + Gf_v(u_{abc}(k), V_{dc}(k), v_n(k)) \tag{17}$$

with F and G given by

$$F = e^{AT_s}, \ G = A^{-1}(F - I_{8\times 8})B \tag{18}$$

where $I_{8\times 8}$ denotes the 8 x 8 identity matrix. It is easy to see that the discrete-time output vector $y(k)$, defined in the same way as (7), is found via

$$y(k) = [([P^T \ 0_{3\times 6}]x(k))^T \ v_n(k)]^T. \tag{19}$$

Equations (16) - (19) provide a complete discrete-time internal control model, with which the controller can predict the evolution of the output in response to a given input sequence. It should be noted that the model assumes that the DC-link voltage remains constant for the duration of each prediction, i.e. $V_{dc}(k+\ell) = V_{dc}(k), \ \forall \ell \in \{0, 1, ..., N_p - 1\}$, where N_p is the prediction horizon.

B. Filter Resonance Damping

In order to eliminate harmonic content in the vicinity of f_1 from the converter current spectrum, it is necessary to incorporate an AD strategy into the MPDCC algorithm. Because the controller directly regulates the converter currents, it is natural for the AD strategy to act on the converter current reference, i.e. i^*_{abc}.

The majority of resonance damping strategies that have been proposed to date have been developed for PWM-based setups [19], [20], [23], [24]. Generally, these approaches rely on a voltage reference being generated for a PWM stage, and as such are not directly applicable to MPDCC, where the controller directly manipulates the switching state of the converter. A different approach, termed the Virtual Resistance (VR) concept, has also been proposed for PWM-based systems [21]. The VR concept is based on the emulation of passive damping resistors, i.e. *virtual* resistors. However, unlike the MLC and filter-based strategies, the VR strategy acts by modifying the converter current reference through an additive damping component, making it suitable for application to MPDCC. As mentioned in the introduction, the VR concept has been applied to an MV IM drive with some success [30], and has also been incorporated into hysteresis current control- and direct power control-based setups [32], [33].

Consider the $\alpha\beta$-frame s-domain representations of an LCL-filter that are shown in Fig. 2, where it is assumed that the fundamental converter current reference, $i^*_f(s)$, is approximately equal to the actual converter current, i.e. $i^*_f(s) \approx i(s)$, and that the grid-side resistance R_g is negligible [21]. Fig. 2(a) shows the arrangement with a damping resistor R_c in series with the filter capacitor, whilst Fig. 2(b) shows the arrangement with a damping resistor R_c in parallel with the filter capacitor. From inspection of Fig. 2(a), it is immediately apparent that the following is true

$$i^*_f(s) - i_g(s) = \frac{sCv_c(s)}{sR_cC + 1} \tag{20}$$

from which it can be deduced that

$$i^*_f(s) + sR_cC(i^*_f(s) - i_g(s)) - i_g(s) = sCv_c(s). \tag{21}$$

If the series-connected damping resistor R_c is now removed from the filter, it is apparent that its effects can be emulated via the inclusion of an additive converter current reference term, $i^*_{vr}(s)$, such that

$$i^*_f(s) + i^*_{vr}(s) - i_g(s) = sCv_c(s) \tag{22}$$

where

$$i^*_{vr}(s) = sR_{vr}Ci_c(s) \tag{23}$$

where R_{vr} is the value of the *virtual* series-connected damping resistor, and where the capacitor current $i_c(s) = i^*_f(s) - i_g(s)$. Similarly, for the arrangement shown in Fig. 2(b), it can be said that

$$i^*_f(s) - i_g(s) = \frac{sR_cCv_c(s) + v_c(s)}{R_c} \tag{24}$$

from which it subsequently follows that

$$i^*_f(s) - \frac{v_c(s)}{R_c} - i_g(s) = sCv_c(s) \tag{25}$$

which has the same form as (21) and (22). Accordingly, the effects of a parallel-connected damping resistor can be emulated in the same manner as a series-connected damping resistor, where $i^*_{vr}(s)$ is given by

$$i^*_{vr}(s) = -\frac{v_c(s)}{R_{vr}}. \tag{26}$$

The two expressions yielding additive reference components, (23) and (26), can easily be converted to the continuous-time-domain, yielding expressions of the form

$$i^*_{vr} = R_{vr}C\frac{di_c}{dt} \tag{27}$$

for the emulation of a resistor in series with the filter capacitor, or

$$i^*_{vr} = -\frac{v_c}{R_{vr}} \tag{28}$$

for the emulation of a resistor in parallel with the filter capacitor. Either of the terms given by (27) and (28) can be incorporated into the MPDCC-VR algorithm to achieve damping of the resonance frequency f_1.

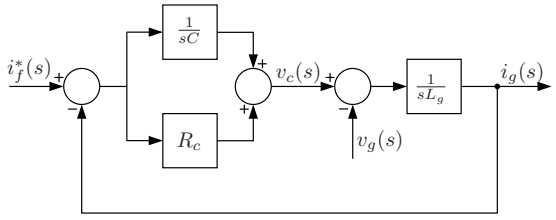

(a)

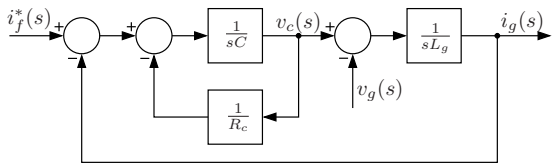

(b)

Fig. 2: s-domain block diagram representations of an LCL-filter with a damping resistor (a) in series with and (b) in parallel with the capacitor.

C. Attenuation of Grid Harmonics

Because the grid currents are regulated implicitly, it is necessary for any harmonics that are present in the grid voltage to be compensated for. The impact of low-frequency harmonics on the performance of LCL-filter-based systems has received some attention, see e.g. [25], and although several strategies have been proposed for PWM-based setups, very little literature has addressed the issue in the context of direct (i.e. modulator-less) control strategies. In [32], [33], a harmonic attenuation strategy is proposed which involves using a PI controller(s) to eliminate particular harmonic(s). However, the strategy requires the use of several digital filters and multiple coordinate transformations in addition to the controller(s), and it is commented that the harmonics that can be attenuated are limited by the bandwidth of the LCL-filter.

Instead, a harmonic attenuation strategy that is also based on the VR concept is adopted. Intuitively, one can think of the grid current harmonics that are caused by the grid voltage harmonics as arising due to the fact that the same harmonics are not present in the capacitor voltage. Thus, it becomes apparent that the harmonic currents can be reduced by emulating a resistor in series with the grid inductor. Fig. 3 provides an s-domain representation of an LCL-filter with a resistor R_{L_g} in series with the grid-side inductor L_g, where the intrinsic grid resistance, R_g, is again considered to be negligible [21]. It is easy to derive the following expression

$$\frac{i_f^*(s) - i_g(s)}{sC} - R_{L_g} i_g(s) - v_g(s) = sL_g i_g(s) \tag{29}$$

from which it can be seen that

$$\frac{i_f^*(s) - sR_{L_g} C i_g(s) - i_g(s)}{sC} - v_g(s) = sL_g i_g(s). \tag{30}$$

If the harmonic attenuating resistor R_{L_g} is now removed from the filter, it is apparent that its effects can be emulated via the inclusion of an additive converter current reference, $i_{vh}^*(s)$, such that

$$\frac{i_f^*(s) + i_{vh}^*(s) - i_g(s)}{sC} - v_g(s) = sL_g i_g(s) \tag{31}$$

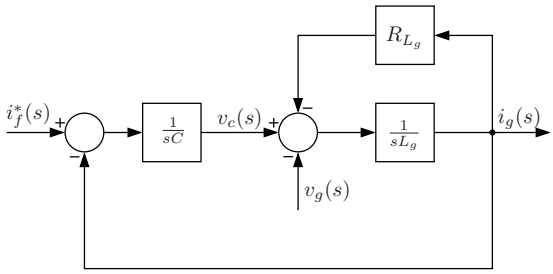

Fig. 3: s-domain block diagram representation of an LCL-filter with a resistor R_{L_g} in series with the grid-side inductor.

where

$$i_{vh}^*(s) = -sR_{vh} C i_g(s) \tag{32}$$

where R_{vh} is the value of the *virtual* harmonic attenuating resistor. Equation (32) can easily be converted to the continuous-time domain, yielding the expression

$$i_{vh}^* = -R_{vh} C \frac{di_g}{dt} \tag{33}$$

which can be incorporated into the MPDCC-VR algorithm to attenuate the harmonics in the grid currents that arise due to the presence of grid voltage harmonics.

D. Control Concept and Reference Generation

As stated in Section II-B, the objective of MPDCC is to regulate the output currents and neutral-point potential within their prescribed bounds, whilst simultaneously minimising the average device switching frequency of the converter. MPDCC utilises a switching horizon, N_s, which is composed of an ordered sequence of events which take place within each prediction: switch, denoted by 'S', and extend, denoted by 'E'. When an 'S' event occurs, the controller has the freedom to switch from the current switching state (input) to a new switching state, advancing the prediction horizon by one time-step. When an 'E' event occurs, the switching state is held constant, with the state and output trajectories extended until violation of the output constraints is predicted to occur, advancing the prediction horizon by a variable number of time-steps. Note that a lower case 'e' event can be included at the beginning of the switching horizon; this represents an 'optional' extension step before the first 'S' event. The fixed switching horizon gives rise to a prediction horizon, N_p, the length of which varies depending on the particular switching sequence under consideration. In order to aid in the explanation of the algorithm, we adopt an additional notation. The number of 'S' events within a switching horizon is defined as S_N, and for a given switching sequence with index j, the points at which switching occurs are denoted $k + \ell_n^j$, $n \in \{0, 1, 2, ..., S_N - 1\}$. If the switching horizon is of the form 'S...E', for instance N_s = 'SESESE', then $\ell_0^j \triangleq 0$, $\forall j$. The formulation of the conventional MPDCC control problem and algorithm is discussed in [18]. Details of the related MPDTC scheme are provided in [3], [12]–[14].

Under the conventional formulation of MPDCC, the dq-frame output current reference, $i_{dq}^*(k)$, is supplied to the

controller at each time-step k, being converted to the abc-frame at each time-step $k+\ell$ within a prediction via

$$i^*_{abc}(k+\ell) = P^T K^T(k+\ell) i^*_{dq}(k+\ell) \tag{34}$$

with

$$i^*_{dq}(k+\ell) \triangleq i^*_{dq}(k), \forall \ell \in \{0, 1, ..., N_p\} \tag{35}$$

and where $K(k+\ell)$ is the $\alpha\beta/dq$ transformation matrix, defined as

$$K(k+\ell) = \begin{bmatrix} cos(\theta(k+\ell)) & sin(\theta(k+\ell)) \\ -sin(\theta(k+\ell)) & cos(\theta(k+\ell)) \end{bmatrix}. \tag{36}$$

The angle $\theta(k+\ell) = \theta(k) + T_s\omega\ell$, where the angle $\theta(k)$ is extracted at each time-step k by a Phase-Locked Loop (PLL), which for a grid-connected converter is aligned with the grid voltage such that $v_{gq} \triangleq 0$.

For the proposed MPDCC-VR strategy, the conventional algorithm is modified to accommodate the resonance damping and harmonic attenuation reference terms. The first step in presenting the new algorithm is converting the additive converter current reference terms to the discrete-time setting of the controller. As stated in Section III-B, either (27) or (28) could be incorporated into the algorithm. However, since it is beneficial to avoid numerical differentiation wherever possible, the use of (28) is preferred.

The resonance damping reference component is updated at a number of time-steps within each prediction, based on the predicted state trajectory. By recalling the definition of the state vector from (11) and the $\alpha\beta/dq$ transformation matrix from (36), then at a given time-step $k+\ell$ within a prediction, the dq-frame resonance damping reference component, $i^*_{dq,vr}(k+\ell) = [i^*_{d,vr}(k+\ell)\ i^*_{q,vr}(k+\ell)]^T$, is given by

$$i^*_{dq,vr}(k+\ell) = -\frac{1}{R_{vr}} K(k+\ell) \begin{bmatrix} x_5(k+\ell) \\ x_6(k+\ell) \end{bmatrix}. \tag{37}$$

Conversely, the harmonic attenuation reference component is treated as being fixed throughout each prediction, and is thus calculated at time-step k only. Again recalling (11) and the $\alpha\beta/dq$ transformation matrix from (36), the dq-frame harmonic attenuation reference component, $i^*_{dq,vh}(k) = [i^*_{d,vh}(k)\ i^*_{q,vh}(k)]^T$, is from (33) given by

$$i^*_{dq,vh}(k+\ell) \triangleq i^*_{dq,vh}(k) = -\frac{R_{vh}C}{T_s} \left(K(k) \begin{bmatrix} x_3(k) \\ x_4(k) \end{bmatrix} - K(k-1) \begin{bmatrix} x_3(k-1) \\ x_4(k-1) \end{bmatrix} \right), \forall \ell \in \{0, 1, ..., N_p\}. \tag{38}$$

Since the fundamental dq-frame converter current reference, $i^*_{dq,f}(k+\ell) = [i^*_{d,f}(k+\ell)\ i^*_{q,f}(k+\ell)]^T$, is also treated as remaining fixed throughout each prediction, i.e.

$$i^*_{dq,f}(k+\ell) \triangleq i^*_{dq,f}(k), \forall \ell \in \{0, 1, ..., N_p\} \tag{39}$$

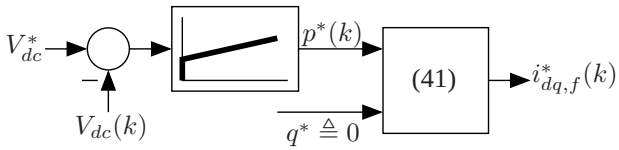

Fig. 4: Fundamental dq-frame converter current reference generation for model predictive direct current control.

the overall dq-frame converter current reference is given at time-step $k+\ell$ within a prediction by

$$i^*_{dq}(k+\ell) = i^*_{dq,f}(k) + i^*_{dq,vh}(k) + i^*_{dq,vr}(k+\ell). \tag{40}$$

Finally, the reference $i^*_{abc}(k+\ell)$ can be computed according to (34), based on $\theta(k+\ell)$ and $i^*_{dq}(k+\ell)$.

The value of $i^*_{dq,f}$ determines the average value of the real and reactive power that are delivered to the grid. It should be noted, however, that $i^*_{dq,f}$ needs to be adjusted to account for the phase shift between the converter and grid currents, and for the DC component of $i^*_{dq,vr}$. By considering both of these factors, and with the real power delivered to the grid given by $p = (3/2)v_{gd}i_{gd}$, it can be shown that the fundamental dq-frame current references are related to the real power reference p^* via

$$i^*_{d,f} = (1 - \omega^2 L_g C + \frac{R_g}{R_{vr}}) \frac{2p^*}{3v_{gd}} + \frac{v_{gd}}{R_{vr}} \tag{41a}$$

$$i^*_{q,f} = \omega(R_g C + \frac{L_g}{R_{vr}}) \frac{2p^*}{3v_{gd}} + \omega C v_{gd} \tag{41b}$$

where v_{gd} is the nominal d-axis grid voltage, and under the assumption that $q^* \triangleq 0$. Due to space constraints, a derivation is omitted. In this work, it is assumed that the DC-link voltage, V_{dc}, is constant, meaning that outer control loops are not needed. However, in practical settings where V_{dc} is not fixed, an outer Proportional-Integral (PI) control loop, as shown in Fig. (4), can be used to generate $p^*(k)$, and therefore $i^*_{dq,f}(k)$, based on the measured value of $V_{dc}(k)$ and the DC-link voltage reference, V^*_{dc}.

E. Control Algorithm

A block diagram illustrating the proposed MPDCC-VR setup is provided in Fig. 5. Note that we treat only $i^*_{dq,f}(k)$ as being supplied to the MPDCC-VR block as an external reference, with the other components of (40) being computed within the MPDCC-VR block. The MPDCC-VR algorithm can be summarised as follows.

1) Initialise a 'Last-In First-Out' stack with the root node, which consists of the previous switching state, $u_{abc}(k-1)$, the measured state vector, $x(k)$, the measured neutral-point potential, $v_n(k)$, and the switching horizon, N_s. If the first element of the horizon is an 'e', duplicate the root node and add it to the stack, discarding the 'e' from the switching horizon of the top node.
2) Calculate the dq-frame current reference $i^*_{dq}(k) = i^*_{dq,f}(k) + i^*_{dq,vh}(k) + i^*_{dq,vr}(k)$, based on the measured state $x(k)$ and the formula for the additive reference components given in (37) and (38).

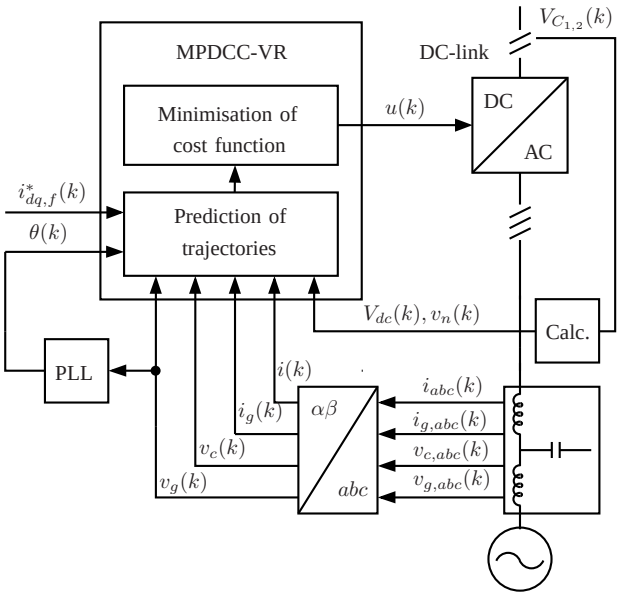

Fig. 5: Setup for MPDCC-VR for a three-phase neutral-point-clamped converter connected to the grid via an LCL-filter.

3a) Take the top node with a non-empty switching horizon from the stack.

3b) Execute and remove the first element of the switching horizon:

- For 'S', update the predicted reference, $i^*_{dq}(k+\ell^j_n) = i^*_{dq,f}(k) + i^*_{dq,vh}(k) + i^*_{dq,vr}(k+\ell^j_n)$, where $n \in \{0,1,2,...,S_N-1\}$, based on the measured or predicted state vector $x(k+\ell^j_n)$. Use the internal control model to predict the state, neutral-point potential and output at $k+\ell^j_n+1$ for each allowable switching state that can be applied at $k+\ell^j_n$. If a switching sequence is a candidate, add it to the top of the stack to form a new node. A candidate switching sequence is one for which each output is either within its bounds, or moving closer to its reference, at $k+\ell^j_n+1$.
- For 'e' or 'E', extend the state, neutral-point potential and output trajectories while holding the switching state, and converter current reference i^*_{dq}, constant, for as long as each output remains a candidate. Extension can be achieved using either the internal control model or an interpolation or extrapolation technique [34].

3c) If there are nodes on the stack with non-empty switching horizons, return to 3a).

3d) If there are no nodes on the stack with non-empty switching horizons, stop.

4) Compute the cost for each candidate input sequence $U^j(k) = [u^j_{abc}(k)\ ...\ u^j_{abc}(k+N^j_p-1)]$, $j \in \mathcal{J}_c$, where $\mathcal{J}_c$ contains the indices of all candidate input sequences. The cost is given by [18]

$$c^j = \frac{1}{N^j_p}\sum_{\ell=0}^{N^j_p-1} ||u^j_{abc}(k+\ell) - u^j_{abc}(k+\ell-1)||_1. \quad (42)$$

5) Determine the switching sequence with the minimal cost

$$j = \arg\min_{j\in\mathcal{J}_c} c^j. \quad (43)$$

6) Apply the switching state $u_{abc}(k) = u^j_{abc}(k)$ and shift the horizon one step forward.

At the next time-step a new optimal switching state $u_{abc}(k+1)$ is determined, based on the measured state, $x(k+1)$ and neutral-point potential, $v_n(k+1)$.

F. Comments

The concept of reference prediction is the key advantage of the MPDCC-VR algorithm. If it was assumed that the resonance damping reference, $i^*_{dq,vr}$, remained equal to the value calculated at time-step k throughout each prediction, the validity of the prediction would decrease with long switching horizons. Whilst it might also be beneficial to update $i^*_{dq,vh}$ throughout each prediction, such an approach would require the non-fundamental component of the grid voltage to also be predicted accurately, which the discrete-time state equation does not accommodate, as can be seen from (13).

The proposed approach is suitable for use with both exact extension and extrapolation-based extension due to the fact that the converter current reference is only updated at 'S' events, at which points the measured or predicted state is always known, rather than during 'E' events, where the predicted state is only known if exact extension is used. A subtle detail which should be noted is that if the switching horizon is of the from 'S...E', then updating the reference at $(k+\ell^j_0)$ is redundant, due to the fact that under such circumstances, $\ell^j_0 \triangleq 0$, i.e. $x(k) = x(k+\ell^j_0)$.

Finally, it should be noted that the MPDCC-VR strategy features the same basic structure as the conventional MPDCC algorithm, and one of the main characteristics of the conventional strategy - namely, the improvement in performance that is exhibited when the switching horizon is lengthened - is preserved with MPDCC-VR, as will be shown in the next section.

IV. Simulation Results

A. Case Study

In this section, we provide simulation results to verify the applicability of the proposed MPDCC-VR scheme to a high-power, MV grid-connected NPC converter. The system is rated to 3 kV, 6.72 MVA; other ratings and parameters are provided in the appendix. The resonant frequency of the LCL-filter is f_1 = 205 Hz, at which point the gain between the converter and grid currents is 38 dB. The sampling interval is fixed at T_s = 100 μs and the neutral-point potential bound width is fixed at δ_{v_n} = 0.03 p.u.. Linear Extrapolation (LE) is used for extension steps. Further details on LE can be found in [34].

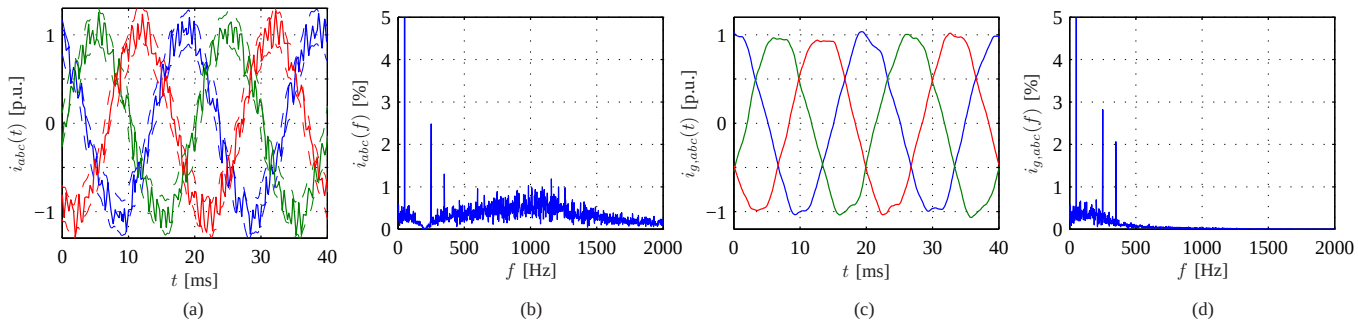

Fig. 6: Simulated converter currents and bounds (a), converter current spectrum (b), grid currents (c), and grid current spectrum, (d), for the proposed MPDCC-VR strategy with N_s = 'eSE', without harmonic attenuation.

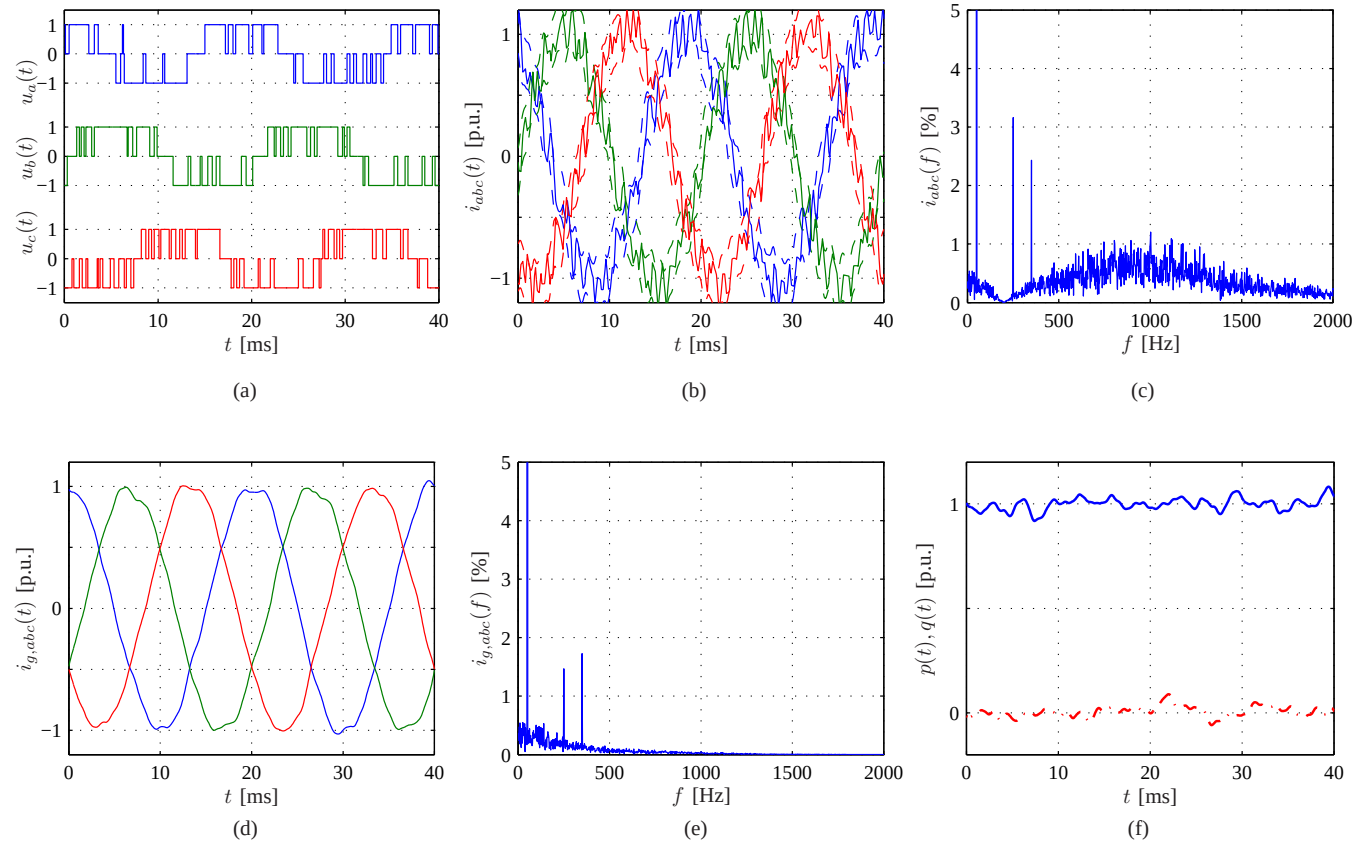

Fig. 7: Simulated switching states (a), converter currents and bounds (b), converter current spectrum (c), grid currents (d), grid current spectrum (e), and real (blue, solid) and reactive (red, dashed) power (f), for the proposed MPDCC-VR strategy with N_s = 'eSE', with harmonic attenuation.

Under steady state operation p^* = 1 p.u., q^* = 0 p.u. is used. In order to consider the simulated performance of the controller under non-ideal conditions, we introduce harmonic distortion to the grid voltage, with 5$^{\text{th}}$ and 7$^{\text{th}}$ harmonic components with magnitudes of 0.015 p.u. added to the 1 p.u. fundamental grid voltage. The resulting THD of the grid voltage is 2.1%.

B. Steady-State Waveforms

In order to illustrate the effect of grid voltage distortion, Fig. 6 shows the converter and grid currents and spectra that are achieved by the proposed MPDCC-VR scheme with N_s = 'eSE', with R_{vr} = 0.5 p.u. and R_{vh} = 0 p.u., i.e. without harmonic attenuation, and with a converter current bound of δ_i = 0.194 p.u.. Although the resonance damping strategy clearly eliminates spectral content from the vicinity of f_1, the impact of the grid voltage harmonics on both the converter and grid current spectra is evident, with peaks at 250 and 350 Hz being present. When averaged over 0.5 s the converter current THD is 13.62%, whilst the grid current THD is 5.84 %.

Fig. 7 shows the waveforms that are obtained when the harmonic attenuation strategy is activated with R_{vh} = 0.35 p.u.. Fig. 7 shows the converter switching states, converter currents and spectrum, grid currents and spectrum, and real and reactive power delivered to the grid over two fundamentals. The impact of the harmonic attenuation strategy on the grid current spectrum is evident, with smaller peaks at 250 and 350 Hz being present in Fig. 7(e) than in Fig. 6(d). The

action of the resonance damping term is again evident from the spectrum of the converter currents, which shows that very little harmonic content in the range of f_1 is present. The real and reactive power are well-regulated, both showing small amounts of ripple. When averaged over 0.5 s, the average device switching frequency is 344 Hz, the converter current THD is 14.83%, and the grid current THD is 4.37%. The increase in converter current THD that is caused when the harmonic attenuation strategy is activated can be observed by comparing Figs. 6(b) and 7(c); it is obvious that the peaks in the converter current spectrum at 250 and 350 Hz increase in the latter, which by recalling Section III-C is necessary for the corresponding grid voltage harmonics to be compensated for.

In order to demonstrate the performance improvement that can be achieved by extending the switching horizon, Table I summarises the performance of the proposed MPDCC-VR strategy with the switching horizons N_s = 'eSE', 'eSSE' and 'eSSESE'. In each case, R_{vr} = 0.5 p.u. and R_{vh} = 0.35 p.u. is used, whilst the width of the converter current bound is adjusted to achieve a grid current THD, $i_{g,THD}$, of 4.5 $\pm$ 0.2 %. In addition, the performance of MPDCC-VR is compared against MLC with SVM. MLC is one of the main strategies that has been applied to the control of grid-connected converters with LCL-filters, and as such forms a valid benchmark against which to compare the proposed MPDCC-VR strategy. The control structure is formulated according to that described in [19], where the outer PI gains are K_p = 0.5 and K_i = 100, and where the inner gain is K_p = 0.4. The SVM stage is implemented with a carrier waveform in the manner described in [35]. The carrier frequency, f_c, determines the switching frequency of the converter, and is adjusted in order to achieve approximately the same level of THD as MPDCC-VR.

At the chosen operating point, the average device switching frequency of MLC with SVM is 450 Hz. With N_s = 'eSE', the switching frequency of MPDCC-VR is 344 Hz, which is 23.6% lower than MLC with SVM. With N_s = 'eSSE', the switching frequency is reduced to 314 Hz, which is 30.2% lower than MLC with SVM, and with N_s = 'eSSESE', the switching frequency is further reduced to 293 Hz, which is 34.9% lower than MLC with SVM. Note also the corresponding increase in the average prediction horizon (in time-steps), N_p^{av}, as the switching horizon is lengthened. The results demonstrate that the proposed MPDCC-VR strategy is robust to moderate levels of grid voltage distortion, and even with a short switching horizon is capable of substantially improving upon the conventional MLC strategy with SVM. Furthermore, it can be seen that by extending the switching horizon, very low device switching frequencies can be achieved whilst remaining within the acceptable limits of individual grid current harmonics and THD, as defined in [31].

TABLE I: Simulated steady-state performance comparison of MLC with SVM and MPDCC-VR.

Control scheme	Control setting	N_s	N_p^{av}	$i_{g,THD}$ [%]	f_{sw} [Hz]
MLC	f_c = 850 Hz	-	-	4.62	450
MPDCC-VR	δ_i = 0.194 p.u.	eSE	4	4.37	344
MPDCC-VR	δ_i = 0.196 p.u.	eSSE	7	4.48	314
MPDCC-VR	δ_i = 0.196 p.u.	eSSESE	11	4.61	293

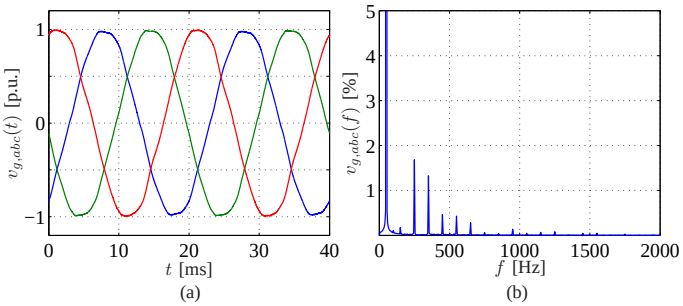

Fig. 8: Experimental grid voltages (a) and spectrum (b).

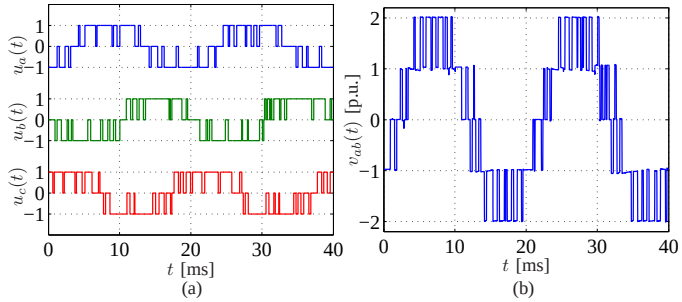

Fig. 9: Experimental switching states (a) and line-to-line converter voltage (b).

V. Experimental Results

A. Setup

In this section, experimental results are provided in order to validate the practical applicability of the MPDCC-VR strategy. Results have been obtained using a down-scaled 240 V, 1.68 kVA system, with additional parameters provided in the appendix. Because the p.u. values of the experimental prototype very closely match those of the MV setup, and because the same values of f_{sw} and $i_{g,THD}$ are used, direct comparison with the results obtained in simulation is possible. The three-phase grid voltage waveforms and spectrum are shown in Fig. 8; the corresponding THD of the grid voltage is similar to that used in simulation.

The DC-link is fed from a constant-voltage power supply. The upper and lower DC-link capacitor voltages and the abc-phase currents and voltages are directly sampled and fed to the controller. The control algorithm is implemented on the 150 MHz TMS320F28335 Digital Signal Processor (DSP). Gate signal and dead-time generation is handled by an Altera Cyclone II Field-Programmable Gate Array (FPGA). Due to the limited processing power of the available hardware platform, experimental results were obtained with N_s = 'eSE', whilst the sampling interval and extrapolation strategy are the same as those used in simulation. Delay compensation as discussed in [13] is used. The same steady-state operating point that was used in simulation is retained, i.e. p^* = 1 p.u., q^* = 0 p.u., and the neutral-point potential bound width remains at δ_{v_n} = 0.03 p.u..

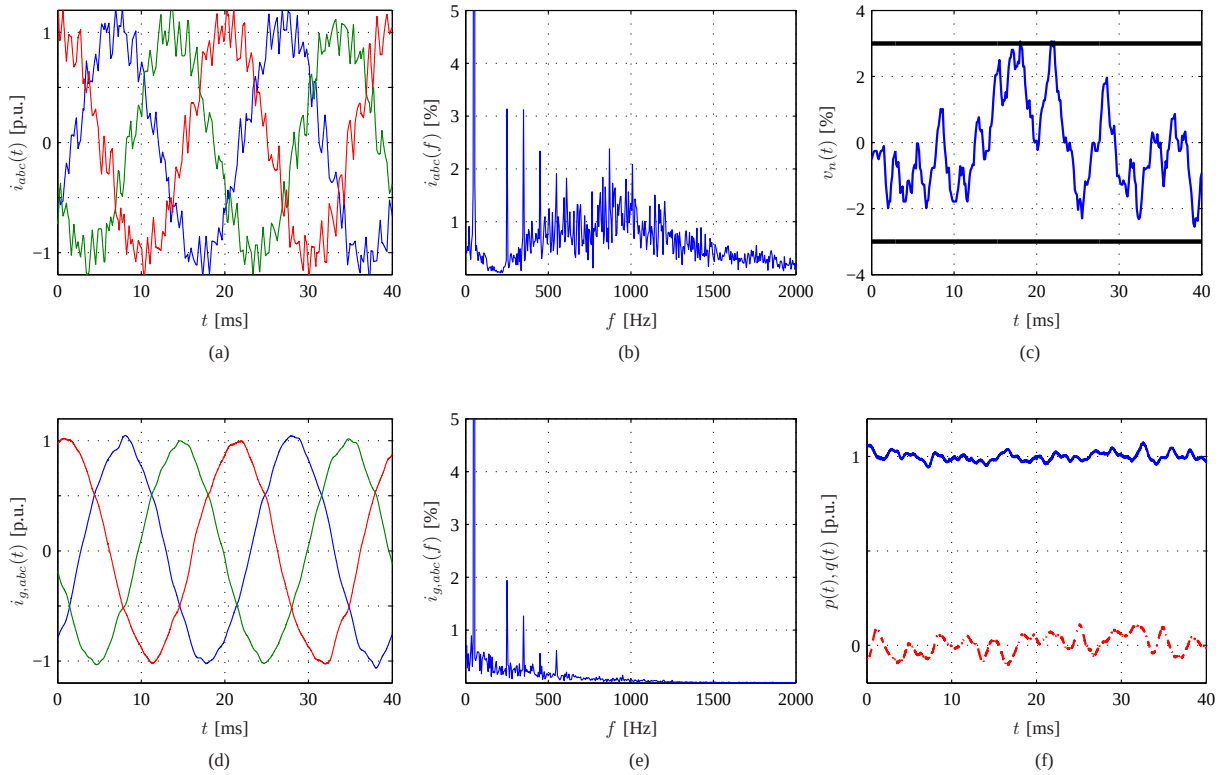

Fig. 10: Experimental converter currents (a), converter current spectrum (b), neutral-point potential and bounds (c), grid currents (d), grid current spectrum (e), and real and reactive power (f), for the proposed MPDCC-VR strategy with N_s = 'eSE'.

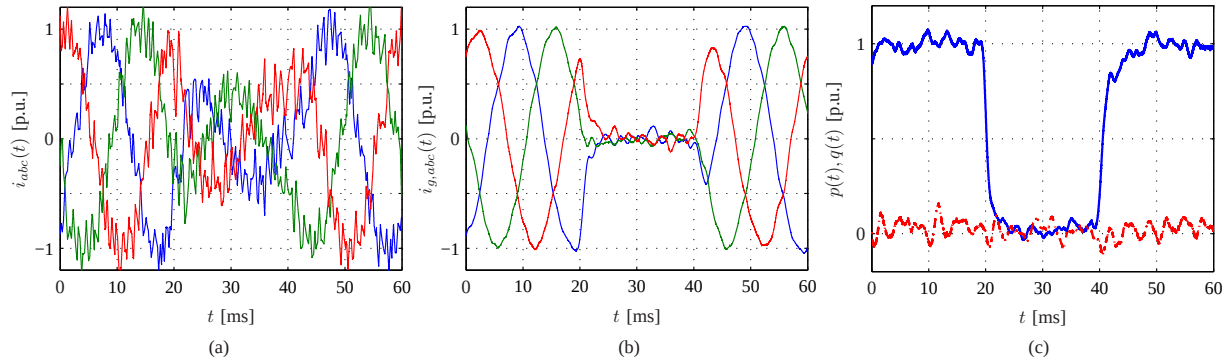

Fig. 11: Experimental converter currents (a), grid currents (b), and real and reactive power (c), for the proposed MPDCC-VR strategy under transient conditions with N_s = 'eSE'.

B. Steady-State Waveforms

Due to the effects of calibration error, sensor delay etc., it was found that the experimental current bound had to be narrowed from 0.194 p.u. to 0.184 p.u. in order to operate at approximately the same switching frequency and grid current THD as in simulation. Fig. 9 shows the switching state and phase-a to phase-b converter voltage, v_{ab}, over two fundamentals. From Fig. 9(a), it can be seen that rapid bursts of switching are avoided, and from Fig. 9(b) it can be seen that the line-to-line voltage is well-balanced, demonstrating that the neutral-point potential is properly regulated by the controller. When averaged over 0.2 s, the average device switching frequency was measured as 341 Hz, which is very similar to the 344 Hz that was achieved in simulation.

Fig. 10 shows the converter currents and spectrum, neutral-point potential, grid currents and spectrum, and real and reactive power, over two fundamentals. From Fig. 10(b), it can be seen that the resonance damping strategy is very effective in eliminating spectral content in the vicinity of f_1 from the converter current spectrum. The regulation of the neutral-point potential is shown in Fig. 10(c). The grid currents, shown in Fig. 10(d), are smooth, and the spectrum, shown in Fig. 10(e), is similar to that seen in simulation. There is no spike at f_1 and the peaks at the main harmonic frequencies are restricted to less than 2%. The real and reactive power, shown in Fig. 10(f), are properly regulated about their reference values with a small amount of ripple being present. When averaged over 0.2 s, the converter current THD is 16.35%, whilst the grid

current THD is 4.40%, which is very close to the 4.37% that was observed in simulation.

C. Transient Waveforms

Fig. 11 shows the transient response of MPDCC in the presence of reference steps. At $t \approx 20$ ms, the real power reference drops from 1 to 0 p.u.. From Figs. 11(a) and 11(b), it can be seen that the converter and grid currents respond quickly and without overshoot. The real and reactive power are shown in Fig. 11(c). The real power reaches its desired level in about 3.5 ms. At $t \approx 40$ ms, the real power reference changes back from 0 to 1 p.u.. The converter currents, grid currents and real power again exhibit a good response, the latter reaching its desired level within about 5 ms. These results demonstrate that the proposed controller achieves a good transient response, and further underline the efficacy of the resonance damping strategy. Despite the excitation of the filter resonance during the reference steps, oscillations at f_1 are kept to a minimum.

D. Discussion

In industrial power electronic systems, inductance and capacitance values can vary over time, which in the case of MPDCC-VR may result in discrepancy between the physical system and the internal control model. Although such mismatch, e.g. grid inductance variation, has not been considered in this work, MPC is, in general, robust to parameter variation. The robust stability of conventional MPDCC was demonstrated in [36], and one could consider MPDCC-VR in the same way. It is very important, however, to note that the proposed resonance damping and harmonic attenuation strategies are not tuned to particular frequencies; consequently, it can be expected that the performance of both strategies will remain similar in the presence of parameter variation or variable grid conditions, which is a major advantage of the proposed strategy.

For the results presented this paper, the values of the virtual resistors R_{vr} and R_{vh} were determined empirically, such that operation at the desired point was achieved. In future, it may be of interest to examine the tuning of MPDCC-VR analytically, as the introduction of R_{vr} and R_{vh} makes the tuning process more complex than that of conventional MPDCC, where δ_i is the primary tuning parameter.

VI. Conclusion

This paper has addressed the problem of developing a long-horizon MPC strategy for the control of MV grid-connected converters with LCL-filters. A new variant of MPDCC, which addresses the issues of resonance damping and harmonic attenuation through the VR concept, has been proposed as a solution for this problem. The resulting control strategy, MPDCC-VR, was discussed in detail, and the new algorithm, which incorporates predictive references, was presented. Simulation results were provided in order to verify the applicability of the MPDCC-VR strategy to a MV case study. The steady-state performance of MPDCC-VR was compared against that of MLC with SVM, and it was shown that MPDCC-VR is capable of offering significantly lower switching frequencies, even when a short switching horizon is used. Experimental results validated the practical viability of MPDCC-VR, with the performance of the down-scaled prototype showing excellent agreement with the results obtained in simulation.

Appendix

The nominal and p.u. parameters of the MV and LV systems are provided in Table II.

TABLE II: Ratings and parameters of the MV and LV LCL-filter-based setup.

Ratings and Parameters			
Quantity	MV value	LV value	p.u. value
DC-link voltage, V_{dc}	5 kV	400 V	2.041
DC-link capacitance, C_{dc}	10 mF	390 mF	4.200
Grid line-to-line voltage, V_g	3 kV	240 V	1.225
Grid current, I_g	1.29 kA	4.04 A	0.707
Grid power, P_g	6.72 MVA	1.68 kVA	1.000
Grid frequency, f	50 Hz	50 Hz	1.000
Converter-side inductance, L	0.567 mH	14.5 mH	0.133
Converter-side resistance, R	10 mΩ	0.25 Ω	0.008
Capacitance, C	1.1 mF	43.3 μF	0.466
Grid-side inductance, L_g	0.567 mH	14.5 mH	0.133
Grid-side resistance, R_g	10 mΩ	0.25 Ω	0.008

References

[1] J. Rodriguez, M. Kazmierkowski, J. Espinoza, P. Zanchetta, H. Abu-Rub, H. Young, and C. Rojas, "State of the art of finite control set model predictive control in power electronics," *IEEE Trans. Ind. Informat.*, vol. 9, no. 2, pp. 1003–1016, May 2013.

[2] D. Quevedo, R. Aguilera, and T. Geyer, "Predictive control in power electronics and drives: Basic concepts, theory, and methods," in *Adv. Int. Contr. Power Electron. Drives*, ser. Studies in Computational Intelligence. Springer International Publishing, 2014, vol. 531, pp. 181–226.

[3] T. Geyer, G. Papafotiou, and M. Morari, "Model predictive direct torque control - part I: Concept, algorithm and analysis," *IEEE Trans. Ind. Electron.*, vol. 56, no. 6, pp. 1894–1905, Jun. 2009.

[4] H. Miranda, P. Cortes, J. Yuz, and J. Rodriguez, "Predictive torque control of induction machines based on state-space models," *IEEE Trans. Ind. Electron.*, vol. 56, no. 6, pp. 1916–1924, Jun. 2009.

[5] C. Rojas, J. Rodriguez, F. Villarroel, J. Espinoza, C. Silva, and M. Trincado, "Predictive torque and flux control without weighting factors," *IEEE Trans. Ind. Electron.*, vol. 60, no. 2, pp. 681–690, Feb. 2013.

[6] P. Cortes, G. Ortiz, J. Yuz, J. Rodriguez, S. Vazquez, and L. Franquelo, "Model predictive control of an inverter with output LC filter for UPS applications," *IEEE Trans. Ind. Electron.*, vol. 56, no. 6, pp. 1875–1883, Jun. 2009.

[7] S. Larrinaga, M. Vidal, E. Oyarbide, and J. Apraiz, "Predictive control strategy for DC/AC converters based on direct power control," *IEEE Trans. Ind. Electron.*, vol. 54, no. 3, pp. 1261–1271, Jun. 2007.

[8] Y. Zhang, W. Xie, Z. Li, and Y. Zhang, "Low-complexity model predictive power control: Double-vector-based approach," *IEEE Trans. Ind. Electron.*, vol. 61, no. 11, pp. 5871–5880, Nov. 2014.

[9] J. Rodriguez, J. Pontt, C. Silva, P. Cortes, U. Amman, and S. Rees, "Predictive current control of a voltage source inverter," *IEEE Trans. Ind. Electron.*, vol. 54, no. 1, pp. 495–503, Feb. 2007.

[10] T. Geyer and D. Quevedo, "Multistep finite control set model predictive control for power electronics," *IEEE Trans. Power Electron.*, vol. 29, no. 12, pp. 6836–6846, Dec. 2014.

[11] T. Geyer and D. Quevedo, "Performance of multistep finite control set model predictive control for power electronics," *IEEE Trans. Power Electron.*, vol. 30, no. 3, pp. 1633–1644, Mar. 2015.

[12] T. Geyer, "Low complexity model predictive control in power electronics and power systems," Ph.D. dissertation, Automatic Control Laboratory, ETH Zurich, 2005.

[13] G. Papafotiou, J. Kley, K. Papadopoulos, P. Bohren, and M. Morari, "Model predictive direct torque control - part II: Implementation and experimental evaluation," *IEEE Trans. Ind. Electron.*, vol. 56, no. 6, pp. 1906–1915, Jun. 2009.
[14] T. Geyer, "Generalized model predictive direct torque control: Long prediction horizons and minimization of switching losses," in *Proc. IEEE Conf. Decis. Control*, Shanghai, China, Dec. 2009, pp. 6799 – 6804.
[15] T. Geyer, "Computationally efficient model predictive direct torque control," *IEEE Trans. Power Electron.*, vol. 26, no. 10, pp. 2804–2816, Oct. 2011.
[16] T. Geyer, "A comparison of control and modulation schemes for medium-voltage drives: Emerging predictive control concepts versus PWM-based schemes," *IEEE Trans. Ind. Appl.*, vol. 47, no. 3, pp. 1380–1389, May/Jun. 2011.
[17] J. Scoltock, T. Geyer, and U. Madawala, "A comparison of model predictive control schemes for MV induction motor drives," *IEEE Trans. Ind. Informat.*, vol. 9, no. 2, pp. 909–919, 2013.
[18] T. Geyer, "Model predictive direct current control: Formulation of the stator current bounds and the concept of the switching horizon," *IEEE Ind. Appl. Mag.*, vol. 18, no. 2, pp. 47–59, Mar. 2012.
[19] E. Twining and D. Holmes, "Grid current regulation of a three-phase voltage source inverter with an LCL input filter," *IEEE Trans. Power Electron.*, vol. 18, no. 3, pp. 888 – 895, May 2003.
[20] P. Loh and D. Holmes, "Analysis of multiloop control strategies for LC/CL/LCL-filtered voltage-source and current-source inverters," *IEEE Trans. Ind. Appl.*, vol. 41, no. 2, pp. 644–654, Mar./Apr. 2005.
[21] P. Dahono, "A control method to damp oscillation in the input LC filter of AC-DC PWM converters," in *Proc. IEEE Power. Electron. Spec. Conf.*, Cairns, Australia, Jun. 2002, pp. 1630 – 1635.
[22] J. Dannehl, F. Fuchs, S. Hansen, and P. ThÃŷgersen, "Investigation of active damping approaches for PI-based current control of grid-connected pulse width modulation converters with LCL filters," *IEEE Trans. Ind. Appl.*, vol. 46, no. 4, pp. 1509–1517, Jul./Aug. 2010.
[23] M. Liserre, A. Aquila, and F. Blaabjerg, "Genetic algorithm-based design of the active damping for an LCL-filter three-phase active rectifier," *IEEE Trans. Power Electron.*, vol. 19, no. 1, pp. 76–86, Jan 2004.
[24] J. Dannehl, M. Liserre, and F. Fuchs, "Filter-based active damping of voltage source converters with LCL filter," *IEEE Trans. Ind. Electron.*, vol. 58, no. 8, pp. 3623–3633, Aug. 2011.
[25] Y. Jia, J. Zhao, and X. Fu, "Direct grid current control of LCL-filtered grid-connected inverter mitigating grid voltage disturbance," *IEEE Trans. Power Electron.*, vol. 29, no. 3, pp. 1532–1541, Mar. 2014.
[26] S. Mariethoz and M. Morari, "Explicit model-predictive control of a PWM inverter with an LCL filter," *IEEE Trans. Ind. Electron.*, vol. 56, no. 2, pp. 389–399, Feb. 2009.
[27] S. Almer, S. Mariethoz, and M. Morari, "Sampled data model predictive control of a voltage source inverter for reduced harmonic distortion," *IEEE Trans. Contr. Syst. Techn.*, vol. 21, no. 5, pp. 1907–1915, Sept 2013.
[28] H. Miranda, R. Teodorescu, P. Rodriguez, and L. Helle, "Model predictive current control for high-power grid-connected converters with output LCL filter," in *Proc. IEEE Ind. Electron. Soc. Conf.*, Porto, Portugal, Nov. 2009, pp. 633–638.
[29] R. Meyer, A. Zlotnik, and A. Mertens, "Fault ride-through control of medium-voltage converters with LCL filter in distributed generation systems," *IEEE Trans. Ind. Appl.*, vol. 50, no. 5, pp. 3448–3456, Sep. 2014.
[30] S. Mastellone, G. Papafotiou, and E. Liakos, "Model predictive direct torque control for MV drives with LC filters," in *Proc. Eur. Conf. Power Electron. Appl.*, Barcelona, Spain, Sep. 2009, pp. 1 – 10.
[31] *IEEE recommended Practices and Requirements for Harmonic Control in Electrical Power Systems*, IEEE 519-1992 Std., 1993.
[32] L. Serpa, S. Ponnaluri, P. Barbosa, and J. Kolar, "A modified direct power control strategy allowing the connection of three-phase inverters to the grid through LCL filters," *IEEE Trans. Ind. Appl.*, vol. 43, no. 5, pp. 1388 – 1400, Sep./Oct. 2007.
[33] L. Serpa, S. Round, and J. Kolar, "A virtual-flux decoupling hysteresis current controller for mains inverter systems," *IEEE Trans. Power Electron.*, vol. 22, no. 5, pp. 1766 – 1777, Sep. 2007.
[34] Y. Zeinaly, T. Geyer, and B. Egardt, "Trajectory extension methods for model predictive direct torque control," in *Proc. IEEE Appl. Power Electron. Conf. Expo.*, Fort Worth, USA, Mar. 2011, pp. 1667 – 1674.
[35] B. P. McGrath, D. G. Holmes, and T. Lipo, "Optimized space vector switching sequences for multilevel inverters," *IEEE Trans. Power Electron.*, vol. 18, no. 6, pp. 1293–1301, Nov. 2003.
[36] T. Geyer, R. Aguilera, and D. Quevedo, "On the stability and robustness of model predictive direct current control," in *Proc. IEEE Int. Conf. Ind. Techn.*, Cape Town, South Africa, Feb. 2013, pp. 374–379.

James Scoltock (S'10) graduated with the B.E. (Hons) degree in electrical and electronic engineering from The University of Auckland, New Zealand, in 2010. He is currently a Ph.D. candidate in electrical and electronic engineering at the same university. His research interests include power electronics, electrical drives and model predictive control.

Tobias Geyer (M'08 - SM'10) received the Dipl.-Ing. and Ph.D. degrees in electrical engineering from ETH Zurich, Zurich, Switzerland, in 2000 and 2005, respectively.

From 2006 to 2008, he was with the High Power Electronics Group of GE's Global Research Centre, Munich, Germany, where he focused on control and modulation schemes for large electrical drives. Subsequently, he spent three years at the Department of Electrical and Computer Engineering, The University of Auckland, Auckland, New Zealand, where he developed model predictive control schemes for medium-voltage drives. In 2012, he joined ABB's Corporate Research Centre, Baden-Dättwil, Switzerland. His research interests are at the intersection of power electronics, modern control theory, and mathematical optimization. This includes model predictive control and medium-voltage ac drives.

Dr. Geyer received the Second Prize Paper Award at the 2008 IEEE Industry Applications Society Annual Meeting and First Prize Paper Award at the 2013 IEEE Energy Conversion Congress and Exposition. He serves as an Associate Editor of the Industrial Drives Committee for the IEEE TRANSACTIONS ON INDUSTRY APPLICATIONS and as an Associate Editor for the IEEE TRANSACTIONS ON POWER ELECTRONICS. He has authored and coauthored about 100 peer-reviewed publications and patent applications.

Udaya K. Madawala (M'95 - SM'06) received the B.Sc. (Hons.) degree in electrical engineering from the University of Moratuwa, Moratuwa, Sri Lanka, and the Ph.D. degree in power electronics from the University of Auckland, Auckland, New Zealand, in 1987 and 1993, respectively.

After working in industry, he joined the Department of Electrical and Computer Engineering, University of Auckland as a Research Fellow in 1997, where he is an currently an Associate Professor, and his research interests include power electronics, inductive power transfer, and renewable energy.

Dr. Madawala is an active IEEE volunteer, he serves as an Associate Editor for IEEE TRANSACTIONS ON INDUSTRIAL ELECTRONICS and the IEEE TRANSACTIONS ON POWER ELECTRONICS. He is a Member of the Power Electronics Technical Committee of Industrial Electronics Society and the Sustainable Energy Systems Committee of IEEE Power Electronics Society.